Asymmetric Hydrogel Electrolyte Featuring Customized Anode and Cathode Interfacial Chemistry for Advanced Zn-I_2 Batteries

Qun Liu[1], Zhenlu Yu[1], Ke Fan[1], Haitao Huang[1], Biao Zhang[1,]*

[1] Department of Applied Physics, The Hong Kong Polytechnic University, Hung Hom, Hong Kong 999077, China

[*] Corresponding Author. E-mail: biao.ap.zhang@polyu.edu.hk

Abstract

An integrated asymmetric hydrogel electrolyte with tailored composition and chemical structure on the cathode/anode-electrolyte interface is designed to boost the cost-effective, high-energy Zn-I_2 battery. Such a configuration concurrently addresses the parasite reactions on the Zn anode side and the polyiodide shuttle issue afflicting the cathode. Specifically, Zn^{2+}-crosslinked sodium alginate and carrageenan dual network (Carra-Zn-Alg) is adopted to guide the Zn^{2+} transport, achieving a dendrite-free morphology on the Zn surface and ensuring long-term stability. For the cathode side, polyvinyl alcohol strengthened poly(3,4-ethylenedioxythiophene)polystyrene sulfonate hydrogel (PVA-PEDOT) with high conductivity is employed to trap the polyiodide and accelerate electron transfer for mitigating the shuttle effect and facilitating I_2/I^- redox kinetics. Attributing to the asymmetrical architecture with customized interfacial chemistry, the optimized Zn-I_2 cell exhibits superior Coulombic efficiency of 99.84% with negligible capacity degradation at 0.1 A g^{-1} and an enhanced stability of 10000 cycles at 5 A g^{-1}. The proposed asymmetric hydrogel provides a promising route to simultaneously resolve the distinct challenges encountered by the cathode and anode interfaces in rechargeable batteries.

Keywords. Asymmetric, hydrogel electrolyte, Zn-I_2 battery, PVA-PEDOT, Carra-Zn-Alg.

Introduction

Extensive efforts have been made to explore the complement to Li-ion batteries for addressing the sustainability concerns associated with Li scarcity and safety issues arising from the flammable organic electrolytes.[1-7] Zn metal batteries with a mild acidic working environment demonstrate great potential for large-scale energy storage applications, attributed to their intrinsic safety, environmental benignity, affordability, and high theoretical capacity (820 mAh g^{-1}) of metallic Zn anode.[8-11] Among the available cathodes, I_2 accommodates the electrons through the I^-/I_2 conversion reaction, exhibiting a theoretical capacity of 211 mAh g^{-1} with a high operating voltage to achieve appealing energy density. Additionally, abundant I_2 resources in seawater (55 μg L^{-1}) are easily accessible to enable sustainable development.[12] Nonetheless, there are several challenges for Zn-I_2 batteries that must be well-settled. For the anode side, the uncontrollable dendrite growth and severe parasitic reaction significantly affect the stability and reversibility of Zn metal, resulting in performance degradation after long-term cycling.[13, 14] Turning to the I_2 cathode, polyiodides generated during the discharging process can be dissolved into the electrolyte and shuttle toward the anode over time. This triggers the loss of active iodine and dramatically reduces the Coulombic efficiency.[15] Moreover, iodine monomers and polyiodides with inherently low electronic conductivity impede the efficient conversion between I_2 and I^-, leading to sluggish kinetics.[16]

To date, extensive research has been conducted to address the above issues for improving the performance of Zn-I_2 batteries. For instance, modifying the I_2 host using open-structured materials like porous carbon,[17] metal-organic frameworks,[18] Prussian blue analogs[19] and starch[20] have been proven effective in confining polyiodide, while constructing artificial Zn interface like Zeolite[21] and zinc silicate[22] endows Zn anode with elevated lifespan and reversibility. Nevertheless, these unilateral approaches tend to solely enhance the performance of either the iodide cathode or the Zn anode with minimal amelioration for the other side. To synchronously tackle the challenges of both sides, researchers have put forward bilateral

strategies like separator coating and electrolyte optimization.[23, 24] However, the poor adherence of the coatings on the separator will result in detachment and failure after continuous long-term cycling. Turning to the electrolyte design, approaches like developing organic additives[25] and high-concentration electrolytes[26] have greatly enhanced electrochemical stability. Nevertheless, compromise may need to be made as few such strategies could concurrently adapt to the cathode and anode challenges. Considering the limitations of these existing approaches, the effective enhancement strategy for Zn-I_2 cells requires a synergistic incorporation of various functionalities associated with the interfaces (**Figure 1a**).[27, 28] Specifically, the cathode interface necessitates high conductivity and polyiodide capture capability to promote kinetics and suppress the shuttle effect, while dendrite-free growth and corrosion resistance are premises for the Zn interface. Furthermore, it is crucial to maintain the stability and integrity of the electrode-electrolyte interface without severe degradation to ensure the long-term operation of the cell.[29, 30]

Asymmetric electrolyte design offers a promising approach to tackle the cathode and anode challenges simultaneously. For example, oil/aqueous-phase, high/low-concentration, and hydrogel/solid-state electrolyte configurations have demonstrated the synergistic effect for performance improvement of Zn-based cells.[31-33] The potential issues associated with such a design include inferior interfacial contact due to the presence of multi-interfaces and the crossover risks between the two sides of the electrolytes. In this work, we endeavor to advance this strategy by designing an integrated asymmetric electrolyte with various functional polymers that concurrently optimizes the cathodic and anodic interfaces in Zn-I_2 batteries (**Figure 1b**). As a critical part between electrodes, hydrogel electrolytes have been evident to promote stable electrode/electrolytes interface by inhibiting parasitic reactions due to the reduction of active free water molecules.[34] Additionally, hydrogel electrolytes provide an opportunity to engineer various electrode/electrolyte interfaces owing to their versatile framework structure and tailorable electrochemical properties.[35]

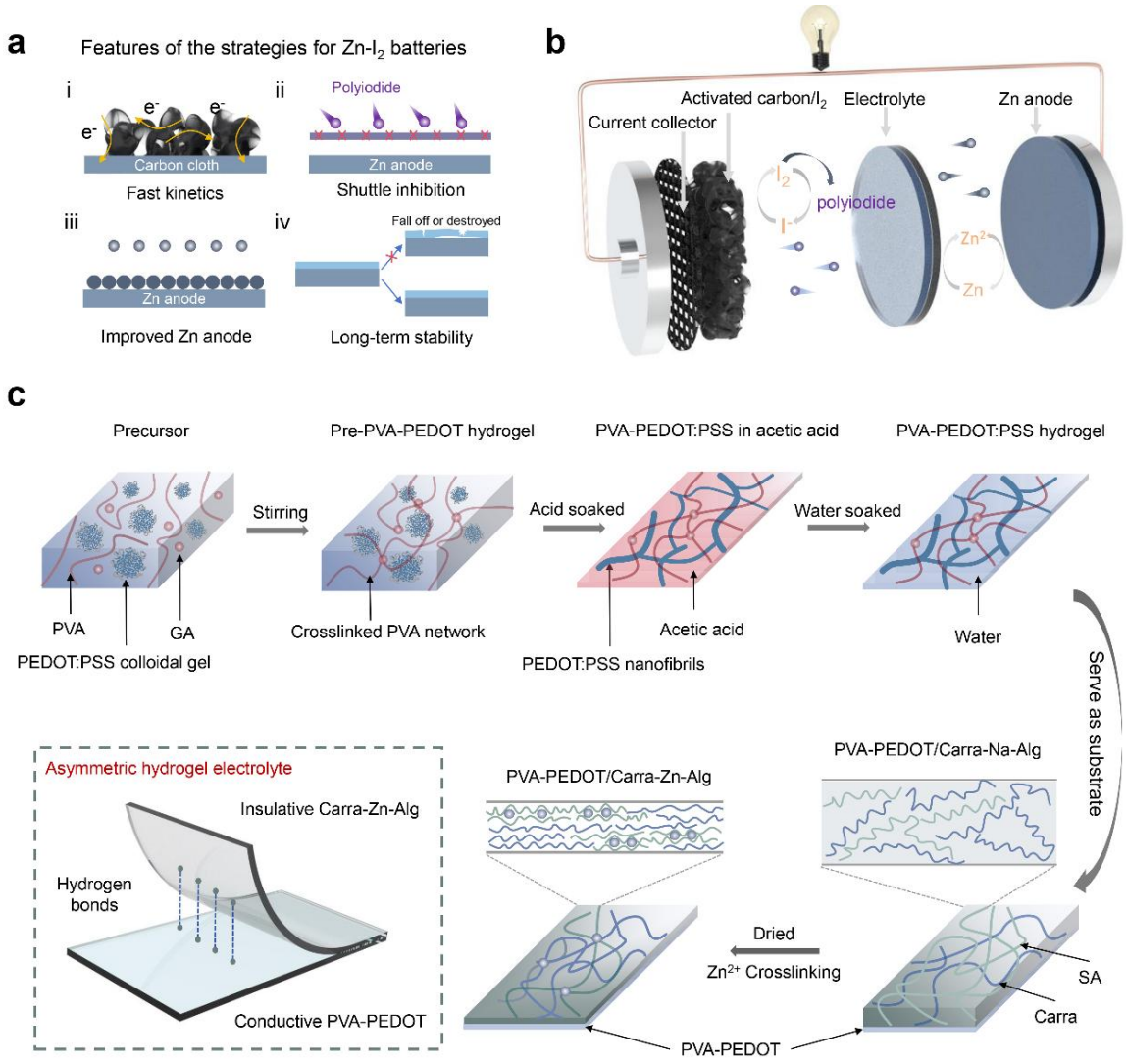

Figure 1. Principle and design of AHE for the Zn-I_2 battery. (a) Features of the strategies for the Zn-I_2 battery; (b) Structure of as-designed Zn-I_2 battery; (c) Preparation process illustration of AHE.

The asymmetric hydrogel electrolyte (AHE) is exploited by integrating polyvinyl alcohol-strengthened poly(3,4-ethylenedioxythiophene) polystyrene sulfonate hydrogel (PVA-PEDOT) with Zn^{2+}-crosslinked sodium alginate and carrageenan dual network (Carra-Zn-Alg). On the cathode side, the PVA-reinforced PEDOT can not only suppress the shuttle effect of polyiodide by strongly interacting with them but also promote the reaction kinetics of I_2 to I^-. Moreover, PEDOT provides an electronic conductive pathway for the reduction/oxidation after capturing the polyiodides with poor electronic conductivity. On the anode side, Carra-Zn-Alg can homogenize Zn^{2+} transfer for dendrite-free deposition, thus realizing improved Zn stability.

Besides, Carra-Zn-Alg exhibits superior mechanical properties with high stiffness and toughness, enhancing the mechanical integrity of the hydrogel electrolyte during cycling.[36] More importantly, its anti-swelling behavior ensures the integrity of AHE when incorporated with PVA-PEDOT. Benefitting from these combined merits, the Zn-I_2 full cell incorporating AHE demonstrates an exceptional Coulombic efficiency of over 99.84% and a long lifespan of 10000 cycles. Furthermore, AHE-based pouch cells with capacities of 15 mAh and 30 mAh exhibit superior stability under extreme test conditions.

Results and discussion

Design and characterization of AHE

Both functionality and integrity should be taken into account for the AHE design. On the one hand, the polymer matrices with specific electrochemical characteristics are desired to meet the individual requirements of the Zn anode and I_2 cathode. On the other hand, the heterojunction inside the hydrogel should be stable during electrode swelling/contraction to prevent creating additional interfaces during cycling. On this basis, the synthesis procedure is elaborated in **Figure 1c**. An integrated structure with different dual-crosslinked polymer networks for the cathode and anode side is prepared. Firstly, PVA, PEDOT:PSS colloidal particles, and glutaraldehyde (GA) were dissolved and reacted in an aqueous solution to form a crosslinked PVA network with PEDOT:PSS colloidal particles dispersed inside (denoted as Pre-PVA-PEDOT hydrogel) (**Figure S1**).[37] Considering that the mechanical strength of such hydrogel is extremely weak ascribed to the low concentration of PVA, acetic acid was selected as a poor solvent to replace the water in Pre-PVA-PEDOT hydrogel and promote the aggregation of PVA networks with PEDOT:PSS colloidal particles.[38] Due to the restriction effect of the PVA network, PEDOT:PSS colloidal particles are constrained to form a continuous conductive nanofibrils network during aggregation. Finally, the dual-network hydrogel was soaked in deionized water to replace acetic acid to form a tough PVA-PEDOT. Noting that with the indispensable acid treatment, a significantly reduced thickness and equivalent area can be

observed (**Figure 2a**), the reason lies in that the lateral movement of polymer chains is restricted by the substrate while vertical movement is unhindered. Without acid treatment, the Pre-PVA-PEDOT hydrogel will directly swell in the aqueous solution and lose mechanical strength (**Figure S2**). A key characteristic of the as-designed PVA-PEDOT hydrogel is its excellent electronic conductivity (1.1 S m^{-1}), which is expected to tackle the kinetics issue of iodine reaction at the cathode interface (**Figure S3**).[39] For the anode-side hydrogel, sodium alginate (SA) and carrageenan (Carra) aqueous solution were cast on PVA-PEDOT substrate (denoted as PVA-PEDOT/Carra-Na-Alg). After being dried and rehydrated in 2 M $ZnSO_4$ aqueous solution, the PVA-PEDOT/Carra-Zn-Alg (AHE) was prepared through SA crosslinking and electrolyte infiltration (**Figure S4**).[40, 41] During the whole process, the loosened Carra-Na-Alg polymers will aggregate and turn into a compact and thin film (**Figure 2b**). Within the asymmetric hydrogel electrolyte, a number of hydrogen bonds between hydroxyl groups and sulfonic acid groups allow the cathode-side and anode-side hydrogels to fit tightly. As illustrated in **Figure S5**, the adhesion energy between the two sides of the electrolyte is 85 J m^{-2}, which ensures interfacial contact.[42] The ionic conductivity of PVA-PEDOT, Carra-Zn-Alg, and integrated AHE are provided in **Figure S6**. It can be found that the integrated design does not have a great impact on the ionic conductivity of AHE, showing great compatibility between the two hydrogel electrolytes.

As displayed in **Figure 2c**, the integrated AHE delivers a small thickness of approximately 50 μm. In addition, cathode-side PVA-PEDOT and anode-side Carra-Zn-Alg both demonstrate a dense and interconnected porous network, which is conducive to mechanical properties (**Figure 2d-e**). As demonstrated in the digital image in **Figure 2f**, the cathode side of the hydrogel shows a dark black color while a transparent state can be observed on the anode side. Such an AHE exhibits superior flexibility which can be freely folded and curled **(Figure S7**). The chemical composition of hydrogel electrolytes was characterized by Fourier transform infrared spectroscopy (**Figure 2g**). Besides the characteristic peaks for Carra-Zn-Alg, C-S

stretching associated with PVA-PEDOT is detected in AHE. In addition, the C-O-C bonding experiences a shift to high wavenumber, resulting from the interaction between Carra-Zn-Alg and PVA-PEDOT.[43] The tight adhesion and integrated features are also reflected in tensile curves (**Figure 2h**). During the tensile process, there is an apparent stress variation under the strain of 40%, attributed to the failure of Carra-Zn-Alg. The smooth stress transition and subsequent maintenance of normal tensile properties evidence the integrity of the AHE without interface damage between Carra-Zn-Alg and PVA-PEDOT under large stress.

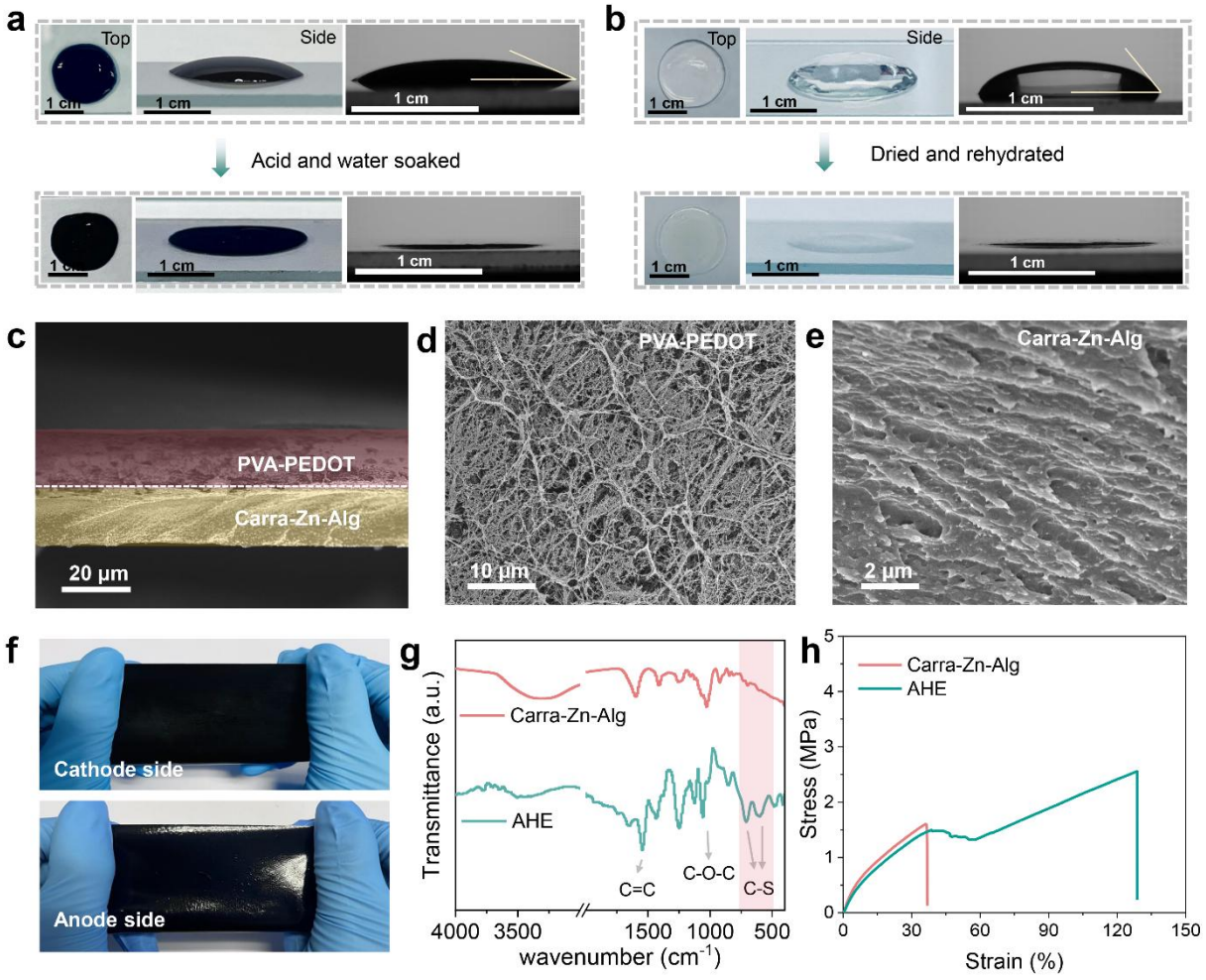

Figure 2. Characterization of AHE. (a) The state of PVA-PEDOT hydrogel before and after acid/H_2O treatment; (b) The state of Carra-Zn-Alg hydrogel before and after reconstruction; (c) Cross-sectional image of AHE; SEM image of (d) PVA-PEDOT and (e) Carra-Zn-Alg hydrogel; (f) Digital images of AHE; (g) FT-IR and (h) Tensile curves of Carra-Zn-Alg and AHE.

Deposition behavior and electrochemical properties of Zn anode with Carra-Zn-Alg

The Zn plating/stripping process tailored by anode-side Carra-Zn-Alg (**Figure S8**) is firstly evaluated by an in situ optical test at a current rate of 5 mA cm^{-2}. As displayed in **Figure 3a**, the Zn anode experiences non-uniform surface evolution in the liquid electrolyte, ultimately leading to the formation of rough and dendritic structures on the anode surface after 60 min. Such uncontrolled growth increases the possibility of cell failure induced by short circuits.[44] In contrast, the Zn anode with Carra-Zn-Alg hydrogel electrolyte maintains a smooth surface during the whole deposition process, which is expected to realize a prolonged lifespan (**Figure 3b**). As a validation, the Zn surface states after the long-term cycling test were further examined. Specifically, after the plating/stripping process in liquid electrolyte for 50 h, Zn dendrites and corrosive byproducts accumulate on the Zn surface, resulting in a porous and loose layer (**Figure 3c**). Additionally, the three-dimensional image taken by confocal laser microscopy (CLSM) shows a height difference of up to 60 μm for the deposited Zn layer (**Figure 3d**), once again proving the rugged surface. On the contrary, the morphology of the Zn anode operated in Carra-Zn-Alg for 100 h remains flat and compact with a much smaller height variation of 24 μm (**Figure 3e-f**), a reflection of the homogeneous deposition.

The distinct deposition behavior is schematically illustrated in **Figure 3g**. Zn^{2+} ions in conventional liquid electrolytes diffuse unevenly across the electrode surface, nucleating at preferred sites with high Zn^{2+} absorption energy, and eventually evolving into undesired dendritic structures. By comparison, the polymer chains with abundant functional groups in Carra-Zn-Alg selectively interact with Zn^{2+} ions and restrict Zn^{2+} ion migration. We examine the interaction between Carra-Zn-Alg and Zn^{2+} through theoretical calculations (**Figure 3h)**. Compared to the lower binding energy of Zn^{2+}-H_2O and Zn^{2+}-Zn, Zn^{2+} exhibits relatively stronger absorption energy with Carra-Zn-Alg, suggesting that the polymer tends to capture Zn^{2+} ions and guide their migration along the chains.[45] In addition, the gradient electrostatic potential (ESP) distribution of Carra-Zn-Alg along polymer chains would facilitate the

directional and homogeneous migration of the Zn^{2+} ions (**Figure S9**). The controllable transport of Zn^{2+} ions from the electrolyte to the Zn anode contributes to uniform morphology evolution which is a premise of long lifespan.

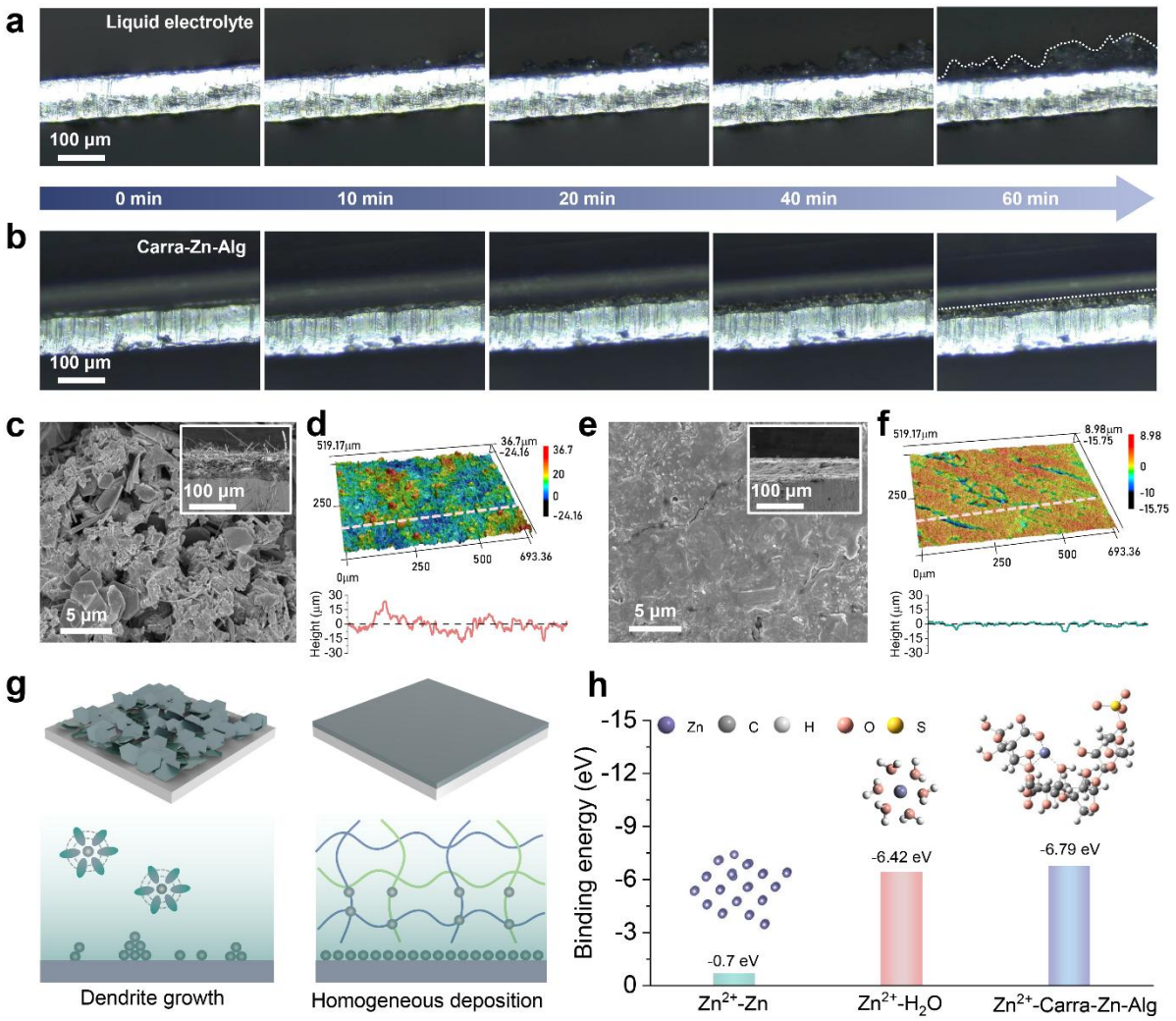

Figure 3. Deposition behavior of Zn anode with Carra-Zn-Alg. In-situ optical images of Zn anode under 5 mA cm^{-2} in (a) liquid electrolyte and (b) hydrogel electrolyte; (c) SEM and (d) CLSM for Zn anode in liquid electrolyte after 50 h; (e) SEM and (f) CLSM for Zn anode in hydrogel electrolyte after 100 h; (g) Schematic illustration of Zn deposition process in various electrolytes; (h) The binding energy between Zn^{2+} and different substances.

Beyond deposition behavior, we further evaluate the electrochemical characteristics of the cell with Carra-Zn-Alg. As shown in **Figure 4a**, the electrochemical window was tested using a three-electrode cell with 1 M Na_2SO_4 as the electrolyte to avoid the interference of Zn

deposition. The Carra-Zn-Alg offers retarded hydrogen and oxygen evolution reactions to suppress the side reactions. The reason lies in the fact the H_2O activity is constrained inside the polymer network.[46]. Additionally, the difference in corrosion states of the Zn anode with distinct electrolytes can be validated by the X-ray diffraction (XRD) pattern (**Figure 4b)**. After cycling for 50 h in the liquid electrolyte, the diffraction peak located at 8.1° appears, attributing to the zinc hydroxide sulfate hydrate ($Zn_4SO_4(OH)_6 \cdot 4H_2O$) on the Zn anode.[47, 48] The absence of such a peak on the Zn anode with Carra-Zn-Alg suggests its superior anti-corrosion capability. To gain a deeper understanding, Zn^{2+} diffusion and transfer features in liquid and hydrogel electrolytes were examined by electrochemical analysis. The dI/dt curves of symmetric Zn//Zn cells were first obtained under a constant overpotential of -150 mV (**Figure 4c)**. It can be observed that the current fluctuates rapidly within 200 seconds for the liquid electrolyte, implying a random Zn^{2+} ions diffusion. By contrast, Carra-Zn-Alg delivers controllable diffusion reflected by a significantly steady-state current.[49] As shown in **Figure S10**, the calculated Zn^{2+} ion transference number for Carra-Zn-Alg (0.59) is considerably higher than the liquid counterpart (0.34), suggesting the improved Zn^{2+} ion transfer kinetics.[50]

The cycling tests of Zn//Zn symmetric cells were subsequently recorded to reveal the effect of Carra-Zn-Alg on the lifespan of the Zn anode. At the current density of 2 mA cm^{-2} and a cycling capacity of 2 mAh cm^{-2}, the cell with liquid electrolyte can be merely operated for about 100 h, followed by a sudden short circuit (**Figure 4d**). By contrast, a prolonged lifespan of over 1200 h with stable voltage profiles can be realized for cells with Carra-Zn-Alg. An analogous result is also obtained under a higher current and capacity of 5 mA cm^{-2}/5 mAh cm^{-2} (**Figure 4e**). By replacing the liquid electrolyte with Carra-Zn-Alg, the cell lifespan was extended from 65 h to 450 h, further proving the applicability of anode-side hydrogel electrolyte. The Zn//Zn symmetric cell with AHE maintains stable voltage for the Zn anode attached to Carra-Zn-Alg, while the Zn toward PVA-PEDOT shows less stability (**Figure S11**). These results indicate the necessity for customized interface design on the anode and cathode.

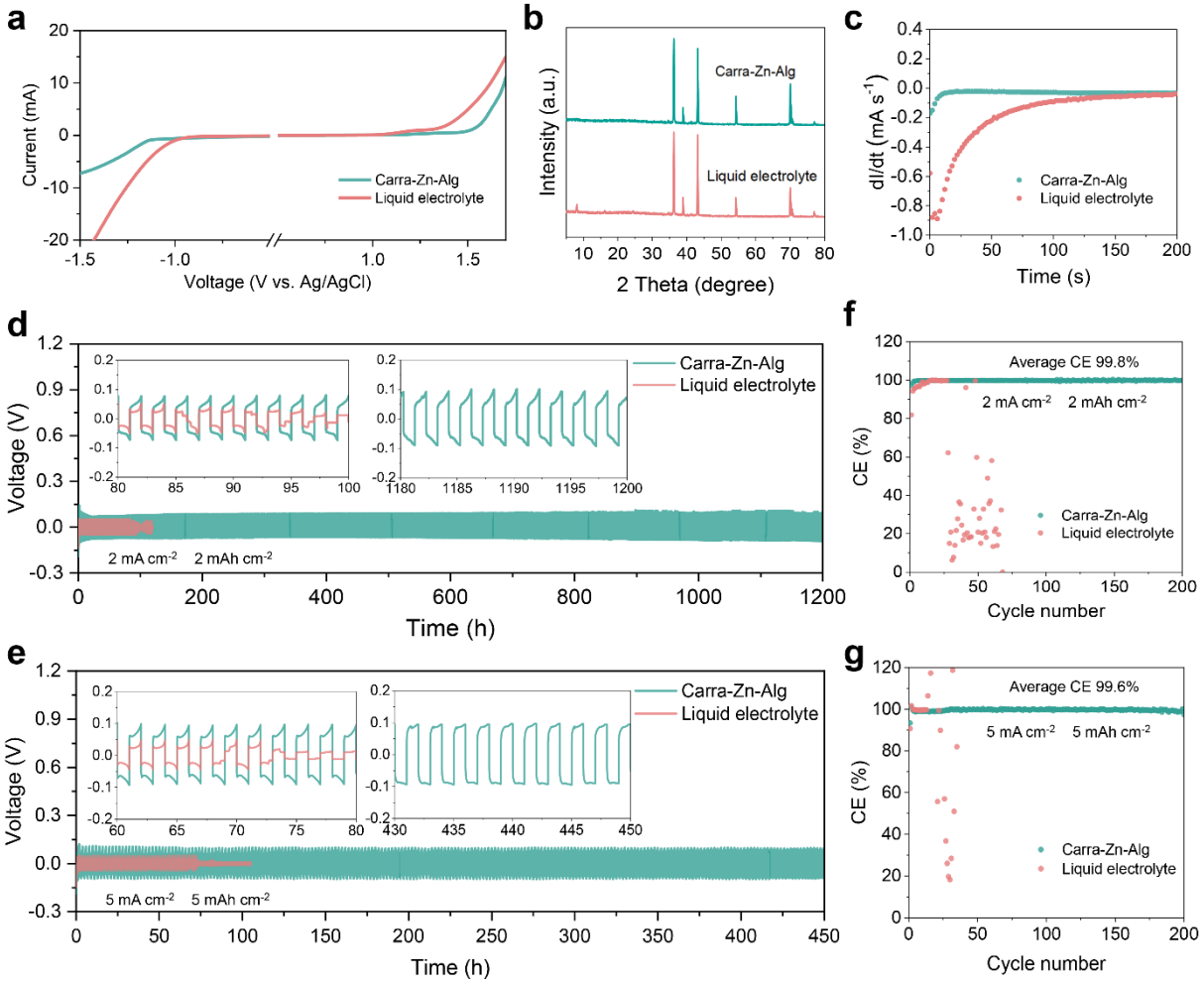

Figure 4. Electrochemical performance. (a) Electrochemical window of Carra-Zn-Alg and liquid electrolyte; (b) XRD pattern of Zn anode after 50 h in various electrolytes; (c) d*I*/d*t* curves under a constant voltage of -150 mV; Voltage profiles of symmetric cells under (d) 2 mA cm^{-2}/2 mAh cm^{-2} and (e) 5 mA cm^{-2}/5 mAh cm^{-2}; Coulombic efficiency of Zn//Cu cell under (f) 2 mA cm^{-2}/2 mAh cm^{-2} and (g) 5 mA cm^{-2}/5 mAh cm^{-2}.

To assess the Zn utilization and reversibility, the asymmetric Zn//Cu cells were assembled to evaluate the Coulombic efficiency (CE).[51] As displayed in **Figure 4f-g**, the CE values experience violent fluctuation after several cycles for the cell with liquid electrolyte attributing to the unstable interfacial reaction. Notably, Carra-Zn-Alg enables an impressive average CE of 99.8% and 99.6% under 2 mA cm^{-2} and 5 mA cm^{-2}, respectively. Such high CE values are solid testaments of optimized Zn reversibility, well consistent with the analysis of dendrite-free deposition and corrosion inhibition.

The effect of AHE on inhibiting polyiodide shuttle effect

After confirming the benefits of Carra-Zn-Alg situating on the anode side of the AHE, we then explore the effect of the integrated hydrogel on inhibiting the shuttle effect of polyiodide. To visualize the polyiodide diffusion, an H-type cell with GF/D, Carra-Zn-Alg, and AHE sandwiched by two chambers was assembled. The catholyte chamber consists of 1 M LiI and 0.1 M I_2 aqueous solution to create I_3^- that simulates the shuttle effect inside the cell. The anolyte chamber is filled with 1 M $ZnSO_4$ aqueous solution. The thickness of all the hydrogel electrolytes is controlled to be 50 μm for fair comparison. When incorporated with a conventional GF/D separator, the colorless solution in the anolyte chamber gradually shifts to light yellow after 20 min and eventually turns completely yellow within 60 min (**Figure 5a**). The phenomenon indicates the unrestricted migration of triiodide across the GF/D film. After replacing GF/D film with Carra-Zn-Alg, the shuttle effect can be alleviated to some extent but cannot be completely suppressed. Impressively, AHE demonstrates exceptional capability against polyiodide shuttle, which is evident by the unchanged states of anolyte solution even after 6 h of aging.[52] The absorbance signals of I_3^- in the right chamber were further measured by ultraviolet-visible spectroscopy (UV/Vis). As shown in **Figure 5b**, GF/D and Carra-Zn-Alg systems exhibit apparent absorbance peaks of penetrated I_3^- after 60 min, while the I_3^- concentration in the cell with AHE was significantly reduced, without detecting prominent signals of I_3^- ions within 6 h. This crossover test illustrates that the adsorption capability of Carra-Zn-Alg may not be sufficient to eliminate the shuttle of polyiodide ions. Instead, the synergistic effect of the PVA-PEDOT and Carra-Zn-Alg effectively confines polyiodide ions on the cathode side, suggesting the necessity of incorporating PVA-PEDOT into AHE.

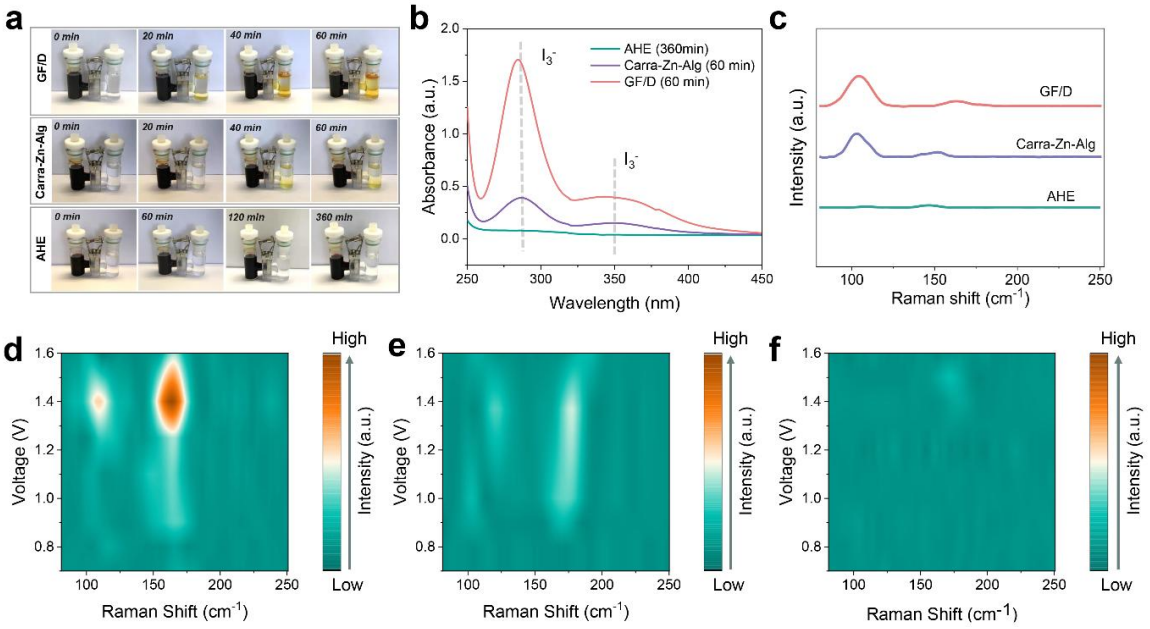

Figure 5. Roles of AHE in inhibiting polyiodides shuttle. (a) Optical images of shuttle effects in a H-cell with I_3^- solution; (b) UV-Vis test of liquid in the right chamber of H-cell; (c) Raman spectrum of Zn anode after self-discharging for 48 h; In situ Raman spectrum of polyiodides on Zn anode during charging process with (d) GF/D, (e) Carra-Zn-Alg and (f) AHE.

To further elucidate the advanced effect of AHE in a real cell system, the assembled Zn-I_2 cell is rested for 48 h to examine the polyiodide signals on the Zn surface (**Figure 5c**). The cell with AHE delivers the minimum peak intensity compared to that of Carra-Zn-Alg and GF/D-based cells, proving the optimal inhibition effect of AHE. We then conducted in situ Raman characterization with a homemade cell (**Figure S12**), which is connected to an electrochemical station for electrochemical tests. During the constant current charging process in various systems, the GF/D-based cell exhibits the strongest polyiodide signal, while the peak intensity is comparatively reduced for the one with Carra-Zn-Alg (**Figure 5d-e**). By contrast, the cell with AHE exhibits negligible polyiodide peaks during the whole process (**Figure 5f**), confirming the effective suppression of intermediate products shuttling from the cathode to the anode. The anode-side hydrogel was separated from the AHE after 50 cycles (**Figure S13**). It can be found that negligible polyiodide signals can be detected, indicating that the crossover has been largely suppressed by PVA-PEDOT. The underlying mechanism is clarified by the

theoretical calculation (**Figure S14**). Compared to anode-side Carra-Zn-Alg, the PEDOT:PSS in cathode-side hydrogel exhibits strong binding energies with polyiodide, in agreement with the Raman results. Gibbs free energy (ΔG) of I_2 reaction pathways was evaluated in **Figure S15**, indicating the spontaneous reduction of I_2 to I^-. The lower ΔG values in AHE for the rate-determining step ($I_3^- \rightarrow I^-$) demonstrate the favorable polyiodide conversion compared with Carra-Zn-Alg. As evidence, the electrochemical impedance spectroscopy (EIS) and galvanostatic intermittent titration technique (GITT) curves of full cells with various electrolytes are tested to study the kinetics of reactions. As shown in **Figure S16**, the EIS plots after cycling reveal that AHE endows the Zn-I_2 full cell with lower charge-transfer resistance (R_{ct}) of 87 Ω compared with the liquid electrolyte (187 Ω) and Carra-Zn-Alg (178 Ω) counterparts, resulting from the promoted I_2 redox reactions and conductive PVA-PEDOT on the cathode side. Furthermore, GITT results indicate that the AHE-based cell shows a higher diffusion coefficient than that of contrast samples arising from improved reaction kinetics (**Figure S17**).

The performance of full cells

Encouraged by the merits of AHE in optimizing Zn anode and trapping polyiodide, the full cell was assembled by pairing the Zn anode with the synthesized I_2 cathode, which was prepared through conventional active carbon (AC) absorption.[53] As revealed in the XRD pattern (**Figure S18**), only the diffraction peaks of AC can be observed, implying that the I_2 is completely confined in the porous structure with an amorphous nature. It should be noted that the AC component in the cathode also contributes a small portion of the capacity (**Figure S19**). The current rates and specific capacities of the full cells were calculated based on the mass of I_2 for easy comparison with previous reports. Thermogravimetric analysis shows an I_2 loading of ~40% (**Figure S20**). The reduction and oxidation behavior of full cells were investigated by cyclic voltammetry (CV) profiles at a scan rate of 0.5 mV s^{-1}. As depicted in **Figure S21**, both

the CV curves of Zn-I_2 cells with liquid electrolyte and AHE show similar shapes with a pair of cathodic/anodic peaks, suggesting the absence of side reactions triggered by the elaborate AHE. When a low current density of 0.1 A g^{-1} is applied for 100 cycles, the Zn-I_2 cell with liquid electrolyte delivers an average CE of 97.25% (**Figure 6a**). The capacity declines to 83.78% of the initial capacity owing to the polyiodide shuttle and Zn anode degradation as confirmed before. In comparison, AHE endows the full cell with an impressive CE of 99.84% and a capacity retention rate of 95.94%. Additionally, the performance of the full cell based on Carra-Zn-Alg under the same condition was also evaluated in **Figure S22a**. As expected, its reversibility and stability lie between the liquid electrolyte and the AHE, illustrating the limitation of monolayer hydrogel film. In terms of the rate performance, the capacity of AHE-based full cell gradually decreases from 210 mAh g^{-1} to 150 mAh g^{-1} when the current rate increases from 0.1 Ag^{-1} to 10 Ag^{-1} (**Figure 6b**). After the current recovers to 0.1 A g^{-1}, the capacities of the full cell return to the nearly initial values, outperforming the cell with liquid electrolyte and Carra-Zn-Alg (**Figure 6c** and **Figure S22b**). Note that the polyiodides transferred to the Zn anode aggravate parasitic reactions and the formation of corrosion products, which destabilizes the overall cell system.[20] As displayed in **Figure S23**, the Zn anode with AHE exhibits negligible corrosion after cycling compared to that with liquid electrolyte and Carra-Zn-Alg.

Regarding long-term stability, the Zn-I_2 cell equipped with AHE delivers an improved CE and stability under 1 A g^{-1} for 1000 cycles (**Figure S24**) and can be operated for a period of 10000 cycles at 5 A g^{-1} with a specific capacity of over 162 mAh g^{-1} (**Figure 6d**). In such an ultralong cycle, the cell shows no more than 15% capacity attenuation, as well as an average charging/discharging efficiency of 99.96%. Impressively, AHE maintains integrity without broken or interfacial damage after long-term cycling (**Figure S25**), showing its excellent stability.[54] Furthermore, a limited Zn deposited on the Cu substrate, with a negative-to-positive electrode capacity (N:P) ratio of 5:1, is adopted as the anode and coupled with the I_2 cathode

for performance evaluation (**Figure 6e**). Benefiting from the positive effects of AHE, the modified Zn-I_2 cell can be operated for 300 cycles with a stale capacity of nearly 170 mAh g^{-1}. In contrast, the capacity for the liquid electrolyte-based cell declines dramatically to 20 mAh g^{-1} after 200 cycles with violent CE fluctuation.

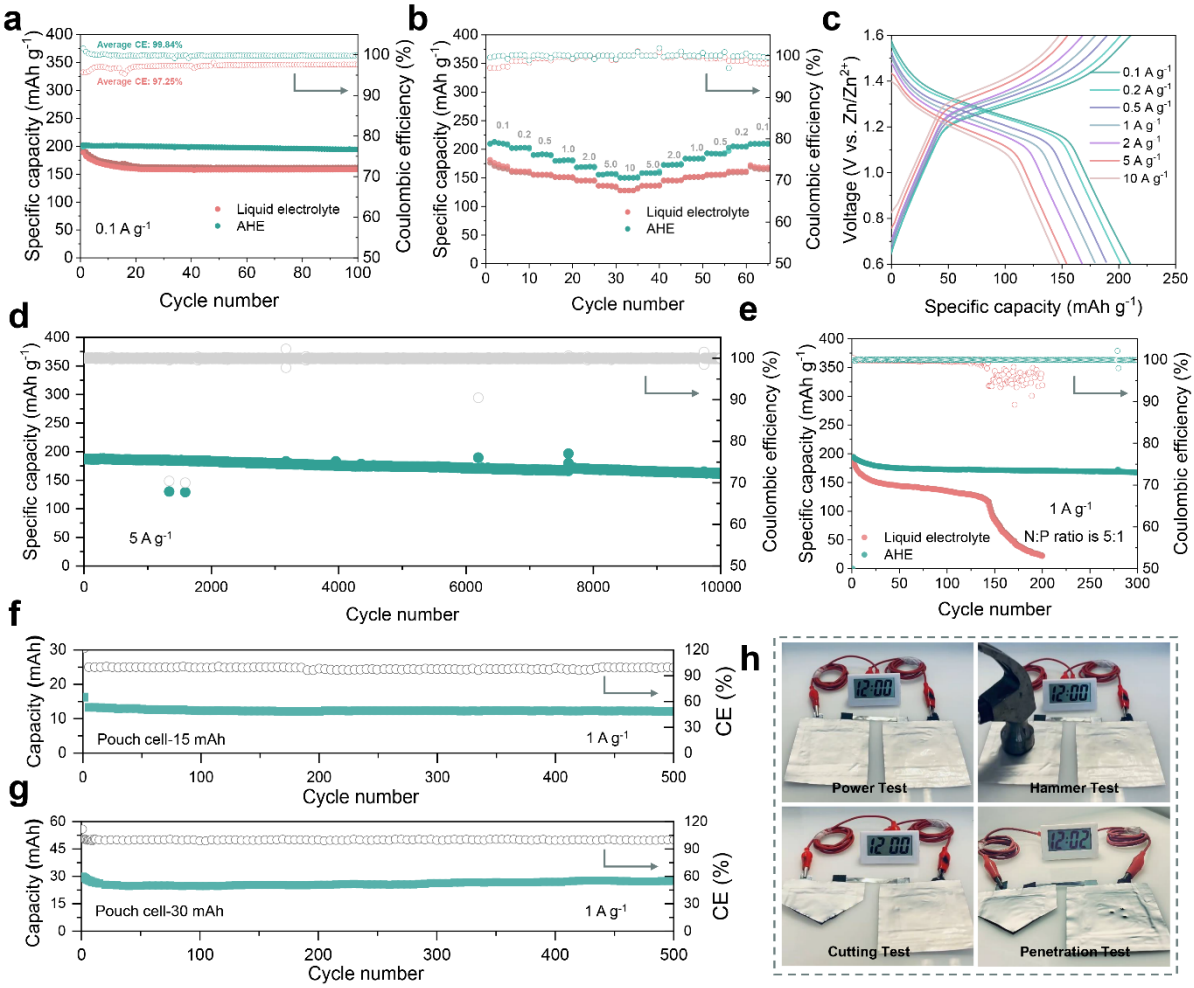

Figure 6. Performance of Zn-I_2 full cell. (a) Cycling performance at 0.1 A g^{-1}; (b) Rate performance from 0.1 A g^{-1} to 10 A g^{-1}; (c) Voltage profiles under various current rates; (d) Cycling performance at 5 A g^{-1}; (e) Cycling performance at 1 A g^{-1} with the N:P ratio of 5:1; (e) Cycling performance of pouch cells with a capacity of (f) 15 mAh and (g) 30 mAh; (h) Digital image of the pouch cells under extreme test conditions.

Impressively, when the mass loading is improved to 10 mg cm^{-2}, the Zn-I_2 coin cell can also be operated stably (**Figure S26**). On this basis, pouch cells with capacities of 15 mAh and 30 mAh were assembled to probe the suitability of AHE for practical applications (**Figure 6f-**

g). After operating for 500 cycles, the capacities remain stable after a slight decrease in the initial several cycles, in line with the results of coin cells. The energy density of the 30 mAh-pouch cell was evaluated according to the detailed parameters presented in **Figure S27**. The calculated energy density is ~30 Wh kg^{-1} under the power density of ~160 W kg^{-1} based on the total mass of active electrodes (including Zn and I_2) and the electrolyte. Considering all the components in the pouch cell, the energy density is ~16 Wh kg^{-1}. It is worth mentioning that the value could be improved by simply reducing the Zn metal thickness and optimizing the package.[55] For instance, an immediate improvement to ~72 Wh kg^{-1} (based on active electrodes and electrolytes) could be obtained by reducing the thickness of Zn foil from 100 to 20 μm (**Figure S28**). With a high I_2 loading of 13.3 mg cm^{-2}, the performance of our pouch cell is competitive among the most recently reported works.[56-58] Inspired by the distinctive safety of the aqueous battery, the working states of pouch cells under extreme test conditions were further evaluated. As demonstrated in **Figure 6h** and **Video S1**, two in-series pouch cells are utilized to drive an electronic clock. Even after undergoing hammering, cutting, and penetration tests, the Zn-I_2 pouch cell remains stable without failure, suggesting its capability to cope with sudden disruption and external stimulation.

Conclusion

An AHE was exploited to tackle various concerns of cathodes and anodes in Zn-I_2 cells. Such hydrogel combines a highly conductive PVA-PEDOT as a cathode-side layer which is tightly adhered to the anode-side layer containing Zn^{2+}-crosslinked sodium alginate and carrageenan. As demonstrated by multiple experimental characterizations and theoretical calculations, the AHE can not only improve redox kinetics of I_2/I^- and inhibit the crossover effect of polyiodide, but also homogenize Zn^{2+} flux and elevate the lifespan of the Zn anode. Consequently, the Zn-I_2 full cell with the elaborated AHE delivers exceptional Coulombic efficiency of 99.84% and improved stability with a 10000-cycle lifespan under 5 A g^{-1}. Moreover, the adaptability of AHE in practical applications is also elucidated by the durability of pouch cells with capacities

of 15 mAh and 30 mAh, which can bear destructive tests without safety hazards. This work offers inspiration to address multiple challenges of Zn-I_2 cells through a holistic approach, which is expected to extend to other complex systems with diverse requirements.

Methods

Preparation of asymmetric hydrogel electrolyte (AHE). The integrated AHE was synthesized through two steps: i). PVA powders (Mw 146,000-186,000) were mixed with PEDOT:PSS colloidal solution (Clevios PH 1000, 1.1-1.3 wt%) with a mass ratio of 1:100, followed by heating at 90 ℃ for 2 h and then cooling down to room temperature. After that, glutaraldehyde was added to the obtained homogeneous solution and stirred for 1h. The precursor was subsequently poured into a polyethylene mold for crosslinking for over 6 h. The as-prepared weak hydrogel was treated with an acetic acid solution and deionized water with a duration of 6 h for each step to form the tough hydrogel (PVA-PEDOT). ii). 1 wt% carrageenan and 1 wt% sodium alginate were dissolved and stirred in deionized water at 90 ℃ for 1 h. The clear solution was immediately transferred to the surface of PVA-PEDOT for preparing PVA-PEDOT/Carra-Na-Alg, which was dried at room temperature for 24 h. Finally, the dried film was removed from the mold and immersed into 2 M $ZnSO_4$ aqueous solution for 1 h to obtain the crosslinked PVA-PEDOT/Carra-Zn-Alg integrated hydrogel electrolyte (denoted as AHE). For comparison, pure Carra-Zn-Alg was prepared on an empty mold using the same method (without PVA-PEDOT as the substrate).

Preparation of the I_2 cathode. Typically, 50 mg I_2 was ultrasonically dissolved in 300 mL of deionized water to form a transparent yellow solution. Then, 50 mg of active carbon was dispersed with magnetic stirring until a dark suspension was formed. The mixture was sealed and rested for at least 24 hours for iodine adsorption. The black products (AC/I_2) were obtained after filtration and drying at room temperature. For the electrode fabrication, AC/I_2, Ketjen

Black and polytetrafluoroethylene (PTFE) were added into isopropanol with a mass ratio of 7:2:1. The homogeneous suspension was coated on carbon cloth and dried at room temperature.

Material characterization. The surface/cross-sectional morphologies and structure of hydrogel samples were characterized by a field emission scanning electron microscope (Tescan MAIA3) and Fourier transform infrared spectrometer (FT-IR, Nicolet iS5). A universal testing machine (Instron 5982) was taken to obtain the tensile properties. Ossila contact angle meter was used to test the states of precursors before and after treatments. Three-dimensional images and surface roughness of Zn anodes were collected by confocal laser microscopy (KEYENCE VK-X150). XRD (Rigaku Smartlab with Cu Kα radiation at 45 kV) was employed to obtain the X-ray diffraction patterns. UV-Vis-NIR spectrometer (PERKIN ELMER) was taken to record UV-vis spectra. Raman spectra were tested by the Witec-Confocal Raman system with an excitation wavelength of 532 nm. For the in-situ Raman test, the spectra were collected through the quartz window of a homemade Raman cell (**Figure S12**), where the charging process was performed by CHI760E. The mass loading of iodine in the cathode was examined by a thermogravimetric analyzer (Rigaku TG/DTA8122). The 90° peeling measurements on hydrogels and electrodes were carried out with a constant peel rate of 10 mm min^{-1} based on an Instron 5967 Tensile Testers.

Electrochemical Tests. CR2032 cells were assembled using AC/I_2 as a cathode, Zn foil as an anode, and as-prepared hydrogels as electrolytes/separators. Besides, cells that sandwich GF/D (Whatman) with 2 M $ZnSO_4$ solution (100 μL) were employed as contrast samples. The specific mass loadings of the I_2 cathode in the coin cell and pouch cell are detailed in **Table S1**. Zn anode lifespan, Coulombic efficiency and galvanostatic charge/discharge profiles were measured by a battery test system (LAND CT2001A). For full-cell tests, the current rates and capacities are determined by the mass of active iodine in the cathode. To ensure the accuracy of the data, at least three batches of samples were tested, showing an error of <5%. EIS, CV, and LSV were performed by the Electrochemical working station (CHI760E). In detail, CV and

LSV were tested at 0.5 and 5 mV s^{-1}, respectively. EIS was examined under a frequency range from 10^5-0.1 Hz.

Computational Methodology. Quantum chemistry calculations were performed using the Gaussian 16 package to optimize molecular geometries of molecules and ion groups. Beck's three-parameter hybrid functional with the Lee-Yang-Parr correlation functional (B3LYP) was used in computations. The LanL2DZ basis set was used for Zn and I ions, and the 6-311+G(d,p) basis set was applied to hydrogen, carbon, nitrogen, oxygen, and sulfur atoms. In addition, the binding energies for these representative structures were calculated at the same level of theory and with Grimme's-D3 (gd3bj) dispersion correction.

Supporting Information. The Supporting Information is available free of charge on the ACS Publications website.

Chemical equation to synthesize PVA and Zn-Alg network; The state of PVA-PEDOT without acid treatment; Electronic conductivity and ionic conductivity of electrolytes; Interfacial toughness of two sides of hydrogel electrolytes; Flexibility demonstration of AHE and Carra-Zn-Alg; ESP distributions of Carra-Zn-Alg; Zn^{2+} transference number in various electrolytes; Voltage profiles of symmetric cell with AHE; Schematic illustration of in situ Raman cell; Raman spectrum of the electrolyte; The binding energy and Gibbs free energy calculation; XRD and TGA tests of AC/I_2 cathode; Cycling performance of AC//Zn cell; EIS, GITT and CV curves of Zn-I_2 full cell; Cycling and rate performance of cell with Carra-Zn-Alg; Optical and SEM images of Zn anode after cycling; Cycling performance of Zn-I_2 full cell at 1 A g^{-1}; Digital images of AHE after cycling; Cycling performance of coin cell with a high I_2 mass loading; The masses of different components in the 30 mAh-pouch cell; Voltage profiles of Zn-I_2 pouch cell with 20 μm Zn foil; Mass loading of cathodes in coin and pouch cells (PDF)

The working states of pouch cells under extreme test conditions (MP4)

Author contributions. B.Z. and Q.L. conceived the idea and designed the experiments. Q.L. and Z.Y. performed the experiments. K.F. carried out the theoretical simulations. B.Z., H.H and Q.L. analyzed the data and prepared this manuscript with inputs from all other coauthors. All authors have given support to the final version of the manuscript.

Notes

The authors declare no competing financial interest.

Acknowledgments

This work was supported by the General Research Fund scheme of the Hong Kong Research Grants Council (Project No. 15307221), the Hong Kong Polytechnic University (YWDF), and PolyU RCNN (Project No. 1-CE0H).

Reference

(1) Liu, B.; Zhang, J. G.; Xu, W. Advancing lithium metal batteries. *Joule* **2018**, 2, 833-845.

(2) Tang, Y.; Zhang L.; Chen, J.; Sun, H.; Yang, T.; Liu, Q.; Huang, Q.; Zhu, T.; Huang, J. Electro-chemo-mechanics of lithium in solid state lithium metal batteries. *Energy Environ. Sci.* **2021**, 14, 602-642.

(3) Harper, G.; Sommerville, R.; Kendrick, E.; Driscoll, L.; Slater, P.; Stolkin, R.; Walton, A.; Christensen, P.; Heidrich, O.; Lambert, S.; Abbott, A.; Ryder, K.; Gaines, L.; Anderson, P. Recycling lithium-ion batteries from electric vehicles. *Nature* **2019**, 575, 75-86.

(4) Tarascon, J.-M.; Armand, M. Issues and challenges facing rechargeable lithium batteries. *Nature* **2001**, 414, 359-367.

(5) Li, M.; Lu, J.; Chen, Z.; Amine, K. 30 years of lithium-ion batteries. *Adv. Mater.* **2018**, 30, e1800561.

(6) Cano, Z. P.; Banham, D.; Ye, S.; Hintennach, A.; Lu, J.; Fowler, M.; Chen, Z. Batteries and fuel cells for emerging electric vehicle markets. *Nat. Energy* **2018**, 3, 279-289.

(7) Fan, X.; Chen, L.; Borodin, O.; Ji, X.; Chen, J.; Hou, S.; Deng, T.; Zheng, J.; Yang, C.; Liou, S. C.; Amine, K.; Xu, K.; Wang, C. Non-flammable electrolyte enables Li-metal

batteries with aggressive cathode chemistries. *Nat. Nanotechnol.* **2018**, 13, 715-722.

(8) Wang, F.; Borodin, O.; Gao, T.; Fan, X.; Sun, W.; Han, F.; Faraone, A.; Dura, J. A.; Xu, K.; Wang, C. Highly reversible zinc metal anode for aqueous batteries. *Nat. Mater.* **2018**, 17, 543-549.

(9) Wang, L.; Huang, K.-W.; Chen, J.; Zheng, J. Ultralong cycle stability of aqueous zinc-ion batteries with zinc vanadium oxide cathodes. *Sci. Adv.* **2019**, 5, eaax4279.

(10) Liu, Q.; Yu, Z.; Zhang, B. Tackling the challenges of aqueous Zn-ion batteries via polymer-derived strategies. *Small Methods*, **2023**, e2300255.

(11) Jia, X.; Liu, C.; Neale, Z. G.; Yang, J.; Cao, G. Active materials for aqueous zinc ion batteries: Synthesis, crystal structure, morphology, and electrochemistry. *Chem. Rev.* **2020**, 120, 7795-7866.

(12) Weng, G.-M.; Li, Z.; Cong, G.; Zhou, Y.; Lu, Y.-C. Unlocking the capacity of iodide for high-energy-density zinc/polyiodide and lithium/polyiodide redox flow batteries. *Energy Environ. Sci.* **2017**, 10, 735-741.

(13) Liu, Q.; Yu, Z.; Zhou, R.; Zhang, B. A semi-liquid electrode toward stable Zn powder anode. *Adv. Funct. Mater.* **2022**, 33, 2210290.

(14) Wang, T.; Wang, T.; Li, C.; Xie, X.; Lu, B.; He, Z.; Liang, S.; Zhou, J. Anode materials for aqueous zinc ion batteries: Mechanisms, properties, and perspectives. *ACS Nano* **2020**, 14, 16321-16347.

(15) Yang, S.; Guo, X.; Lv, H.; Han, C.; Chen, A.; Tang, Z.; Li, X.; Zhi, C.; Li, H. Rechargeable iodine batteries: Fundamentals, advances, and perspectives. *ACS Nano* **2022**, 16, 13554-13572.

(16) Chen, H.; Li, X.; Fang, K.; Wang, H.; Ning, J.; Hu, Y. Aqueous zinc-iodine batteries: From electrochemistry to energy storage mechanism. *Adv. Energy Mater.* **2023**, 13, 2302187.

(17) Liu, M.; Chen, Q.; Cao, X.; Tan, D.; Ma, J.; Zhang, J. Physicochemical confinement effect enables high-performing zinc-iodine batteries. *J. Am. Chem. Soc.* **2022**, 144, 21683-21691.

(18) Chai, L.; Wang, X.; Hu, Y.; Li, X.; Huang, S.; Pan, J.; Qian, J.; Sun, X. In-MOF-derived hierarchically hollow carbon nanostraws for advanced zinc-iodine batteries. *Adv Sci (Weinh)* **2022**, 9, e2105063.

(19) Ma, L.; Ying, Y.; Chen, S.; Huang, Z.; Li, X.; Huang, H.; Zhi, C. Electrocatalytic iodine reduction reaction enabled by aqueous zinc-iodine battery with improved power and energy densities. *Angew. Chem. Int. Ed.* **2021**, 60, 3791-3798.

(20) Zhang, S. J.; Hao, J.; Li, H.; Zhang, P. F.; Yin, Z. W.; Li, Y. Y.; Zhang, B.; Lin, Z.; Qiao, S. Z. Polyiodide confinement by starch enables shuttle-free Zn-iodine batteries. *Adv. Mater.* **2022**, 34, e2201716.

(21) Shang, W.; Li, Q.; Jiang, F.; Huang, B.; Song, J.; Yun, S.; Liu, X.; Kimura, H.; Liu, J.; Kang, L. Boosting Zn||I_2 Battery's performance by coating a zeolite-based cation-exchange protecting layer. *Nanomicro Lett.* **2022**, 14, 82.

(22) Peng, H.; Fang, Y.; Wang, J.; Ruan, P.; Tang, Y.; Lu, B.; Cao, X.; Liang, S.; Zhou, J. Constructing fast-ion-conductive disordered interphase for high-performance zinc-ion and zinc-iodine batteries. *Matter* **2022**, 5, 4363-4378.

(23) Chen, G.; Kang, Y.; Yang, H.; Zhang, M.; Yang, J.; Lv, Z.; Wu, Q.; Lin, P.; Yang, Y.; Zhao, J. Toward forty thousand-cycle aqueous zinc-iodine battery: Simultaneously inhibiting polyiodides shuttle and stabilizing zinc anode through a suspension electrolyte. *Adv. Funct. Mater.* **2023**, 33, 2300656.

(24) Kang, Y.; Chen, G.; Hua, H.; Zhang, M.; Yang, J.; Lin, P.; Yang, H.; Lv, Z.; Wu, Q.; Zhao, J.; Yang, Y. A Janus separator based on cation exchange resin and Fe nanoparticles-decorated single-wall carbon nanotubes with triply synergistic effects for high-areal capacity Zn-I_2 batteries. *Angew. Chem. Int. Ed.* **2023**, 62, e202300418.

(25) Hao, J.; Yuan, L.; Zhu, Y.; Bai, X.; Ye, C.; Jiao, Y.; Qiao, S. Z. Low-cost and non-flammable eutectic electrolytes for advanced Zn-I_2 batteries. *Angew. Chem. Int. Ed.* **2023**, 62, e202310284.

(26) Ji, Y.; Xie, J.; Shen, Z.; Liu, Y.; Wen, Z.; Luo, L.; Hong, G. Advanced zinc-iodine batteries with ultrahigh capacity and superior rate performance based on reduced graphene oxide and water-in-salt electrolyte. *Adv. Funct. Mater.* **2023**, 33, 2210043.

(27) Stamenkovic, V. R.; Strmcnik, D.; Lopes, P. P.; Markovic, N. M. Energy and fuels from electrochemical interfaces. *Nat. Mater.* **2016**, 16, 57-69.

(28) Park, K.; Yu, B.-C.; Jung, J.-W.; Li, Y.; Zhou, W.; Gao, H.; Son, S.; Goodenough, J. B. Electrochemical nature of the cathode interface for a solid-state lithium-ion battery: Interface between $LiCoO_2$ and garnet-$Li_7La_3Zr_2O_{12}$. *Chem. Mater.* **2016**, 28, 8051-8059.

(29) Mohamed, A. I.; Sansone, N. J.; Kuei, B.; Washburn, N. R.; Whitacre, J. F. Using polypyrrole coating to improve cycling stability of $NaTi_2(PO_4)_3$ as an aqueous Na-ion anode. *J. Electrochem. Soc.* **2015**, 162, A2201-A2207.

(30) Lim, H.-S.; Kwak, W.-J.; Chae, S.; Wi, S.; Li, L.; Hu, J.; Tao, J.; Wang, C.; Xu, W.; Zhang, J.-G. Stable solid electrolyte interphase layer formed by electrochemical pretreatment of gel polymer coating on Li metal anode for lithium-oxygen batteries.

ACS Energy Lett. **2021**, 6, 3321-3331.

(31) Chen, S.; Ying, Y.; Ma, L.; Zhu, D.; Huang, H.; Song, L.; Zhi, C. An asymmetric electrolyte to simultaneously meet contradictory requirements of anode and cathode. Nat. Commun. **2023**, 14, 2925.

(32) Chen, A.; Zhan, Y.; Li, Q.; Liang, G.; Yang, S.; Huang, Z.; Yang, Q.; Hu, H.; Li, X.; Chen, Z.; Fan, J.; Zhi, C. An immiscible phase-separation electrolyte and interface ion transfer electrochemistry enable zinc/lithium hybrid batteries with a 3.5 V-class operating voltage. *Energy Environ. Sci.* **2023**, 16, 4054-4064.

(33) Lu, H.; Zhang, D.; Jin, Q.; Zhang, Z.; Lyu, N.; Zhu, Z.; Duan, C.; Qin, Y.; Jin, Y. Gradient electrolyte strategy achieving long-life zinc anodes. *Adv. Mater.* **2023**, 35, 2300620.

(34) Park, J.-H.; Hyun Park, S.; Joung, D.; Kim, C. Sustainable biopolymeric hydrogel interphase for dendrite-free aqueous zinc-ion batteries. *Chem. Eng. J.* **2022**, 433, 133532.

(35) Yang, J. L.; Yu, Z.; Wu, J.; Li, J.; Chen, L.; Xiao, T.; Xiao, T.; Cai, D. Q.; Liu, K.; Yang, P.; Fan, H. J. Hetero-polyionic hydrogels enable dendrites-free aqueous Zn-I_2 batteries with fast kinetics. *Adv. Mater.* **2023**, 35, e2306531.

(36) Ji, D.; Park, J. M.; Oh, M. S.; Nguyen, T. L.; Shin, H.; Kim, J. S.; Kim, D.; Park, H. S.; Kim, J. Superstrong, superstiff, and conductive alginate hydrogels. Nat. Commun. **2022**, 13, 3019.

(37) Wei, H.; Kong, D.; Li, T.; Xue, Q.; Wang, S.; Cui, D.; Huang, Y.; Wang, L.; Hu, S.; Wan, T.; Yang, G. Solution-processable conductive composite hydrogels with multiple synergetic networks toward wearable pressure/strain sensors. *ACS Sens.* **2021**, 6, 2938-2951.

(38) Lu, B.; Yuk, H.; Lin, S.; Jian, N.; Qu, K.; Xu, J.; Zhao, X. Pure PEDOT:PSS hydrogels. *Nat. Commun.* **2019**, 10, 1043.

(39) Zhang, Y.; Zhao, T.; Yang, S.; Zhang, Y.; Ma, Y.; Wang, Z. Flexible PEDOT:PSS nanopapers as “anion-cation regulation” synergistic interlayers enabling ultra-stable aqueous zinc-iodine batteries. *J. Energy Chem.* **2022**, 75, 310-320.

(40) Zhang, B.; Qin, L.; Fang, Y.; Chai, Y.; Xie, X.; Lu, B.; Liang, S.; Zhou, J. Tuning Zn^{2+} coordination tunnel by hierarchical gel electrolyte for dendrite-free zinc anode. *Sci. Bull. (Beijing)* **2022**, 67, 955-962.

(41) Liu, Q.; Wang, Y.; Hong, X.; Zhou, R.; Hou, Z.; Zhang, B. Elastomer-alginate interface for high-power and high-energy Zn metal anodes. *Adv. Energy Mater.* **2022**, 12,

2200318.

(42) Ye, T.; Wang, J.; Jiao, Y.; Li, L.; He, E.; Wang, L.; Li, Y.; Yun, Y.; Li, D.; Lu, J.; Chen, H.; Li, Q.; Li, F.; Gao, R.; Peng, H.; Zhang, Y. A tissue-like soft all-hydrogel battery. *Adv. Mater.* **2022**, 34, 2105120.

(43) He, F.; You, X.; Gong, H.; Yang, Y.; Bai, T.; Wang, W.; Guo, W.; Liu, X.; Ye, M. Stretchable, biocompatible, and multifunctional silk fibroin-based hydrogels toward wearable strain/pressure sensors and triboelectric nanogenerators. *ACS Appl. Mater. Interfaces* **2020**, 12, 6442-6450.

(44) Aslam, M. K.; Niu, Y.; Hussain, T.; Tabassum, H.; Tang, W.; Xu, M.; Ahuja, R. How to avoid dendrite formation in metal batteries: Innovative strategies for dendrite suppression. *Nano Energy* **2021**, 86, 106142.

(45) Liu, Q.; Yu, Z.; Zhuang, Q.; Kim, J. K.; Kang, F.; Zhang, B. Anti-fatigue hydrogel electrolyte for all-flexible Zn-ion batteries. *Adv. Mater.* **2023**, 35, e2300498.

(46) Yang, J. L.; Li, J.; Zhao, J. W.; Liu, K.; Yang, P.; Fan, H. J. Stable zinc anodes enabled by a zincophilic polyanionic hydrogel layer. *Adv. Mater.* **2022**, 34, e2202382.

(47) Mao, Y.; Li, Z.; Li, Y.; Cao, D.; Wang, G.; Zhu, K.; Chen, G. Breaking intramolecular hydrogen bonds of polymer films to enable dendrite-free and hydrogen-suppressed zinc metal anode. *Chem. Eng. J.* **2023**, 461, 141707.

(48) Zhang, M.; Li, S.; Tang, R.; Sun, C.; Yang, J.; Chen, G.; Kang, Y.; Lv, Z.; Wen, Z.; Li, C. C.; Zhao, J.; Yang, Y. Stabilizing Zn/electrolyte interphasial chemistry by a sustained-release drug inspired indium-chelated resin protective layer for high-areal-capacity Zn//V_2O_5 batteries. Angew. Chem. Int. Ed. 2024, e202405593.

(49) Chen, A.; Zhao, C.; Guo, Z.; Lu, X.; Liu, N.; Zhang, Y.; Fan, L.; Zhang, N. Fast-growing multifunctional $ZnMoO_4$ protection layer enable dendrite-free and hydrogen-suppressed Zn anode. *Energy Storage Mater.* **2022**, 44, 353-359.

(50) Li, C.; Xie, X.; Liang, S.; Zhou, J. Issues and future perspective on zinc metal anode for rechargeable aqueous zinc-ion batteries. *Energy Environ. Mater.* **2020**, 3, 146-159.

(51) Hao, Y.; Feng, D.; Hou, L.; Li, T.; Jiao, Y.; Wu, P. Gel electrolyte constructing Zn (002) deposition crystal plane toward highly stable Zn anode. *Adv. Sci. (Weinh)* **2022**, 9, e2104832.

(52) Lin, P.; Chen, G.; Kang, Y.; Zhang, M.; Yang, J.; Lv, Z.; Yang, Y.; Zhao, J. Simultaneous inhibition of Zn dendrites and polyiodide ions shuttle effect by an anion concentrated electrolyte membrane for long lifespan aqueous zinc-iodine batteries. ACS Nano 2023, 17, 15492-15503.

(53) Chen, M.; Zhu, W.; Guo, H.; Tian, Z.; Zhang, L.; Wang, J.; Liu, T.; Lai, F.; Huang, J. Tightly confined iodine in surface-oxidized carbon matrix toward dual-mechanism zinc-iodine batteries. *Energy Storage Mater.* **2023**, 59, 102760.

(54) Lv, Z.; Kang, Y.; Chen, G.; Yang, J.; Chen, M.; Lin, P.; Wu, Q.; Zhang, M.; Zhao, J.; Yang, Y. Stable solid-state zinc-iodine batteries enabled by an inorganic $ZnPS_3$ solid electrolyte with interconnected Zn^{2+} migration channels. Adv. Funct. Mater. 2024, 34, 2310476.

(55) Li, W.; Ma, Y.; Li, P.; Jing, X.; Jiang, K.; Wang, D. Electrochemically activated $Cu_{2-x}Te$ as an ultraflat discharge plateau, low reaction potential, and stable anode material for aqueous Zn-ion half and full batteries. *Adv. Energy Mater.* **2021**, 11, 2102607.

(56) Li, Z.; Cao, W.; Hu, T.; Hu, Y.; Zhang, R.; Cui, H.; Mo, F.; Liu, C.; Zhi, C.; Liang, G. Deploying cationic cellulose nanofiber confinement to enable high iodine loadings towards high energy and high-temperature Zn-I_2 battery, *Angew. Chem. Int. Ed*. **2024**, 63, e202317652.

(57) Zhang, Y.; Zhang, X.; Li, X.; Chen, C.; Yu, D.; Zhao, G. Enabling high-areal-capacity zinc-iodine batteries: Constructing high-density microporous carbon framework with large surface area. *J. Alloys Compd.* **2024**, 976, 173041.

(58) He, J.; Hong, H.; Hu, S.; Zhao, X.; Qu, G.; Zeng, L.; Li, H. Chemisorption effect enables high-loading zinc-iodine batteries. *Nano Energy* **2024**, 119, 109096.